Journal of Advanced Ceramics
先进陶瓷
ISSN 2226-4108
CN 10-1154/TQ
清华大学出版社 Tsinghua University Press
SciOpen

J Adv Ceram 2026, **15**: 9221415

https://doi.org/10.26599/JAC.2026.9221415

Research Article

Amorphous SiOC nanofibers: A multifunctional platform integrating electromagnetic wave transparency, thermal insulation, and mechanical resilience for extreme environments

Yi Hou [1,2,#], Linghao Pan [1,2,#], Hui Zhang[1,2], Fanqi Meng[1,2], Yan Gao [1,2], Yu Hua [1,2], Mengyue Peng [3], Lixi Wang [1,2,*]

[1]*College of Materials Science and Engineering, Nanjing Tech University, Nanjing 211816, China*

[2]*Jiangsu Collaborative Innovation Center for Advanced Inorganic Function Composites, Nanjing 211816, China*

[3]*Department of Mechanical Engineering, National University of Singapore, Singapore 117575*

[#]These authors contributed to the work equally and should be regarded as co-first authors

*Corresponding authors:

E-mail: wanglixi_njut@163.com

Received: July 24, 2026; Revised: November 17, 2026; Accepted: November 24, 2026

©The Author(s) 2026

Just Accepted

Abstract

Amorphous SiOC ceramics show promise potential for high-temperature electromagnetic wave (EMW) transmission owing to their light weight, low dielectric loss, and thermal/oxidation resistance. However, bulk SiOC suffers from inherent brittleness and poor designability, limiting applications on complex structural surfaces. Herein, flexible amorphous SiOC nanofiber membranes were fabricated via electrospinning by precisely regulating precursor-solution viscosity and conductivity to minimize defects and create free surfaces for stress release. The resulting three-dimensional nanofiber network endows the membranes with exceptional compressive resilience (retaining >95% of initial maximum stress after 500 cycles at 50% strain), ultralow thermal conductivity (<0.04 $W \cdot m^{-1} \cdot K^{-1}$), fire resistance (structural integrity maintained after 5 min flame exposure), and excellent recyclability (negligible mass and adsorption-capacity loss after ten pollutant adsorption–elimination cycles). Moreover, the amorphous SiOC phase yields an ultralow dielectric constant ($\varepsilon' \approx 1.0$) and loss tangent ($\tan \delta < 0.0023$), enabling >99% EMW transparency across the entire X band; this transparency remains above 98% after cyclic compression and high-temperature treatment. These findings offer valuable insights into the design of multifunctional wave-transmitting materials for harsh environments.

Keywords: Amorphous SiOC nanofibers, Electromagnetic wave transmission, Thermal insulation, Fire resistance, Pollutant adsorption, Multifunctional.

1. Introduction

The escalating thermal and electromagnetic challenges confronting hypersonic vehicles necessitate that radome materials maintain excellent electromagnetic wave (EMW)-transmitting performance, mechanical strength, and structural stability under extreme high-temperature conditions. [1, 2] High-temperature EMW-transmitting materials based on Si_3N_4, borate ceramics, and oxides such as Al_2O_3 and ZrO_2 have been reported. [3-5] Compared with wave-transmitting materials based on these traditional ceramic matrices, polymer-derived ceramics (PDCs)[6, 7] have effectively alleviated the intrinsic trade-off between mechanical strength and wave-transmitting performance in conventional high-temperature ceramics, attributable to their customizable dielectric behavior, ultralight structural architecture, outstanding thermo-oxidative resilience, and superior fiber-forming capability. Accordingly, PDCs are regarded as promising candidates for the

Just Accepted

development of next-generation advanced and multifunctionally integrated EMW-transmitting materials. [8-11] These materials are expected to possess a low dielectric constant, low dielectric loss, and thermal insulation properties, while also meeting the demands for lightweight structural design. Consequently, the development of high-temperature-resistant, lightweight, and multifunctionally integrated electromagnetic wave-transmitting materials has become a research focus. [12-14]

PDC-SiOC materials,[15, 16] by virtue of their amorphous structure and tunable nanoscale composition, exhibit outstanding high-temperature resistance (>1000 °C), high strength, chemical stability, and low dielectric loss. These properties render them highly promising candidates for next-generation high-temperature-resistant and multifunctional EMW-transmitting materials.[17-19] However, bulk SiOC ceramics commonly suffer from high brittleness, low fracture toughness, and limited specific surface area, which restrict their engineering applications in complex service conditions. Fiberization and nanosizing of ceramic materials are considered effective strategies to overcome these limitations, as exemplified by $MgAl_2O_4$,[20] Ni/C@ZrO_2,[21] SiC@SiO_2 NFs,[22] and SiC_{nws}/SiOC nanowires[23]. This approach enhances mechanical flexibility and specific surface area through the construction of high-aspect nanoscale fibers, thereby expanding their application potential in electromagnetic functionality, thermal insulation, and multifunctional integration.

Electrospinning is an efficient and controllable technique for producing nanofibers, capable of generating continuous, uniform, and diameter-tunable one-dimensional ceramic nanofibers. It offers significant advantages such as flexible compositional tuning and diverse structural design capabilities.[24, 25] Previous studies have demonstrated that electrospinning ceramic-based nanocomposite fibers, such as ZnO,[26] γ-Al_2O_3,[27] CuO/TiO_2,[28] CS/PVA/POP,[29] and carbon/$Bi_{20}TiO_{32}$/MoS_2/Bi_2S_3,[30] can realize the micro/nanostructures with uniform morphology and consistent size distribution through the optimization of electrospinning parameters, precursor formulation design, or post-treatments such as thermal processing and crosslinking. Electrospun nanofibers exhibit high anisotropy, continuity, and porosity, which significantly reduce membrane density and consequently enhance mechanical performance. Moreover, the tunability of processing parameters enables precise control over fiber diameter and microstructure, affording a favorable platform for functional integration and multi-field responsive properties. However, systematic investigations into the fabrication of SiOC ceramic nanofibers via electrospinning remain limited,

Just Accepted

rending uniform and stable preparation challenging. This has consequently restricted the functional exploration and practical applications of electrospun SiOC ceramic nanofiber membranes across various fields.

Despite significant advances in the fabrication of electrospun ceramic nanofibers and polymer-derived SiOC materials, their practical utilization for radomes and antenna windows still requires multifunctional integrated protection. These components must simultaneously withstand aerodynamic heating, mechanical vibration and deformation, and maintain broadband EM transparency under extreme conditions. Moreover, they are inevitably exposed to environmental pollutants including hydrocarbon deposits, oil mists, and particulate dust, which can adhere to the material surface, alter local dielectric properties, and progressively effect wave-transmission efficiency. Therefore, developing a multi-functional EM transparent candidate with lightweight, mechanical resilient and pollutant recyclable properties remains a critical challenge.

Herein, we have proposed a synergistic design paradigm for multifunctional wave-transparent ceramics that operates across three interconnected levels. Architecturally, the electrospun 3D porous nanofiber network establishes a lightweight, highly porous scaffold in which nanoscale fiber dimensions simultaneously suppress solid-state thermal conduction, provide inter-fiber sliding channels for mechanical energy dissipation, and lower the effective dielectric constant toward that of air. Compositionally, a precisely controlled post-pyrolysis oxidation strategy tailors the free-carbon content within the amorphous Si–O–C backbone: the progressive elimination of conductive carbonaceous phases minimizes dielectric loss and enhances EM transparency, while the retention of the non-crystalline SiOC framework preserves the intrinsic flexibility and damage tolerance of the fibrous matrix. Functionally, this harmonious interplay between structural porosity and compositional tuning enables the monolithic integration of ultrahigh EMW transmission, thermal insulation, compressive resilience, and recyclable pollutant adsorption within a single all-ceramic membrane. As a result, the amorphous microstructure of SiOC phase contributes to an ultra-low dielectric constant ($\varepsilon' \approx 1.0$) and loss tangent ($\tan \delta < 0.0023$), ensuring excellent EMW transparency above 99% with the entire X band, which remains above 98% after cyclic compression and high-temperature treatment. Consequently, the multifunctional and stable performance renders the SiOC nanofibers promising candidates for wave-transmitting materials in complex and harsh serving environments.

Just Accepted

2. Methods

Preparation of electrospinning precursor solution

Firstly, 15 mL of isopropanol and 5 mL of N,N-dimethylformamide (DMF) were mixed in a sealed bottle. Then 1.2 g Polyvinyl pyrrolidone (PVP) was added, and the solution was stirred for 1 h until completely dissolved, 3.4 g of siloxane-based polymers (MK), and 0.135/0.27/0.54 g of $Fe(acac)_3$ were added. After stirring for an additional 3 h, a uniformly mixed electrospinning precursor solution was obtained.

Preparation of SiOC nanofiber membranes

Subsequently, the precursor solution was transferred into a 10 mL plastic syringe without a plunger for electrospinning. During electrospinning, a stainless-steel needle (inner diameter approximately is 0.62 mm) was connected to the syringe, with a flow rate of 0.03 mL/min and a positive voltage of 15 kV. The as-spun MK precursor nanofibers were collected by a low-speed roller rotating at 150 rpm with an applied negative voltage of 5 kV. The distance between the needle tip and the roller collector was 14 cm. At this stage, the modified SiOC precursor nanofibers were prepared. Second, the modified SiOC precursor nanofibers were cured at 190 °C in air for 1 hour at a heating rate of 5 °C/min. The cured nanofibers were further pyrolyzed at 1000 °C in Ar atmosphere for 8 hours at a heating rate of 2.5 °C/min. The sample obtained by adding 0.27 g of the $Fe(acac)_3$ was designated as SF-1000. Thereafter, the thermally treated SF-1000 fiber membranes were subsequently annealed in air at 1000 °C, 1100 °C and 1200 °C for 3 hours, yielding oxidized samples designated as SFO-1000/1100/1200. In addition, the remaining fiber membranes were annealed in air at 1100 °C and designated as $SF_{0.135}O$-1100 and $SF_{0.54}O$-1100 according to the respective additive ($Fe(acac)_3$) amounts.

Table 1 Sample name and the corresponding description

Sample Name	$Fe(acac)_3$ amount (g)	Pyrolysis temp. (°C)	Oxidation temp. (°C)
Pure SiOC	0	1000	/
SF-1000	0.27	1000	/
SFO-1000	0.27	1000	1000
$SF_{0.27}O$-1100 (SFO-1100)	0.27	1000	1100
SFO-1200	0.27	1000	1200
$SF_{0.135}O$-1100	0.135	1000	1100
$SF_{0.54}O$-1100	0.54	1000	1100

Just Accepted

Materials Characterization

The morphology and microstructure of the samples were captured by scanning electron microscopy (SEM, S-4700, Hita-chi, 15 kV) and transmission electron microscopy (TEM, F-30, FEI-Tecnai, 300 kV). An X-ray diffractometer (XRD, Rigaku Ultima IV with Cu Ka radiation), a HORIBA Jobin Yvon Modular Raman Microscope (laser source wavelength of 514 nm) and an X-ray photoelectron spectrometer (XPS, ESCALAB 250Xi) were used to determine the crystal structure, Raman spectra and chemical structure. The compression resilience of SF-1000 and SFO-1100 nanofiber membranes was evaluated using a universal testing machine (Instron 5500, US) at a loading speed of 2 mm/min. The thermal conductivity of the membranes was measured at room temperature using a thermal conductivity meter (TC3000E). The dielectric properties and S-parameters of SF-1000 and SFO-1100 nanofiber membranes were measured at room temperature using an Agilent vector network analyzer. The tests were conducted in the X-band (8.2 ~ 12.4 GHz) using a cuboid membrane with dimensions of 22.8 mm × 10.2 mm and a stacked thickness of 6.5 mm in a waveguide.

In this work, multiple single-layer membranes were stacked for testing. For waveguide-based EM parameter measurement, membranes were die-cut into 22.8 mm × 10.2 mm rectangles and laminated to an overall thickness of 6.5 mm. For thermal insulation, adsorption, and compression assessments, membranes were cut to 30 mm × 30 mm rectangles and stacked to 10 mm in total thickness. No additional binder was applied between adjacent layers. Instead, gentle pressing was employed to achieve natural fiber entanglement. The stacked membranes were then subjected to 10 cycles of 30% strain compression until negligible thickness variation was observed.

3. Results and discussion

3.1 Preparation and nanosizing of amorphous SiOC nanofibers

The one-dimensional (1D) alignment and nanosizing of fibers are critical factors determining the bending stiffness of nanofiber membranes.[31] Reducing fiber dimensions helps minimize macroscopic defects, improve the overall uniformity of ceramic fiber materials, and provide additional free surfaces for stress release, thereby enhancing flexibility.[32, 33] **Fig. 1a** shows the synthesis process of amorphous SiOC nanofiber membranes via electrospinning and high

Just Accepted

temperature treatment. Detailed fabrication information is provided in the **Experimental Section**. The pyrolyzed SiOC nanofibers before and after oxidation are designated as SF and SFO nanofibers, respectively. As shown in **Fig. 1b**, the MK in the precursor membranes undergo pyrolysis to form amorphous SiOC. During subsequent high-temperature oxidation, carbon is consumed while oxygen is incorporated. The as-prepared nanofiber membranes exhibit excellent cuttability to fit various macroscopic configurations (**Fig. 1c**). Additionally, the continuous 1D nanofibers are distributed in a 3D, unoriented manner, contributing to the excellent flexibility and compressive resilience of the membranes (**Fig. 1d-g**). The low mass and density enable the stacked membranes to rest freely on fresh flowers, as shown in **Fig. 1h**. Furthermore, large-area SFO nanofiber membranes can be easily fabricated via electrospinning (**Fig. 1i-j**).

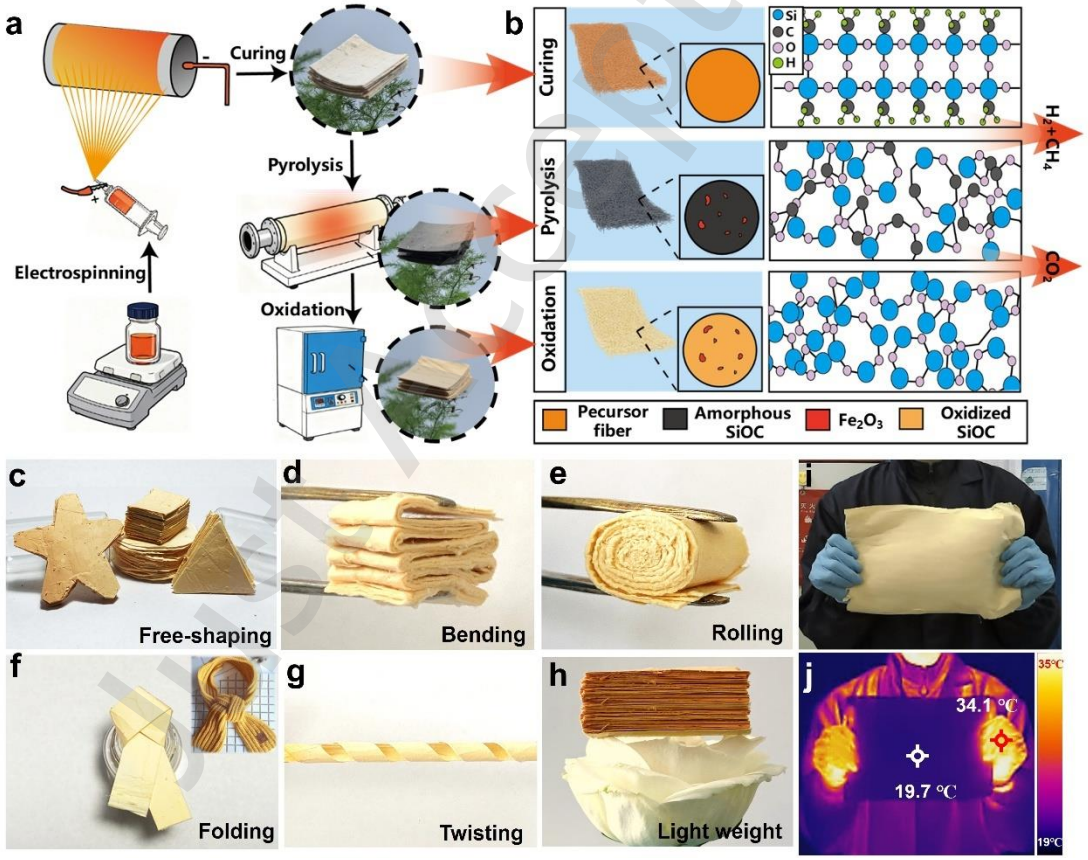


Fig. 1. **(a)** Schematic illustration of the preparation process. **(b)** Molecular structures evolution for the pyrolysis of MK and oxidation of SiOC nanofibers. **(c-h)** Digital photographs demonstrating the free-shaping macrostructure, flexibility and lightweight features of amorphous SiOC nanofiber membranes. **(i-j)** Digital and infrared photographs of large-area nanofiber membranes.

The regulation of viscosity and conductivity in the electrospinning solution plays a key role in the nanosizing of modified SiOC fibers.[34] As shown in **Fig. 2a**, the introduction of MK precursor significantly increased the solution viscosity from 101 to 135 mPa·s, whereas its conductivity

markedly decreased to 0.99 $\mu S \cdot m^{-1}$. As a common additive for modulating solution viscosity and conductivity, iron(III) acetylacetonate ($Fe(acac)_3$) was employed (**Supporting methods**). Its addition effectively decreased almost linearly from 135 mPa·s to 94 mPa·s, whereas the conductivity rapidly increased to 1.84 $\mu S \cdot m^{-1}$. The reduction in viscosity weakened the polymer chain entanglement, facilitating nanofiber formation during electrospinning. Meanwhile, the enhanced conductivity improved solution spinnability. Under the applied electric field, the increased charge density within the electrospinning jet further promoted fiber stretching, ultimately yielding more uniform nanofibers. The three insets in **Fig. 2a** further demonstrate the spinning states under different solution viscosity and conductivity conditions.[35, 36] To achieve the stable fabrication of uniform and continuous SiOC ceramic fibers, a systematic matrix-designed experimental approach was employed to investigate the effects of precursor-solution properties on both the macroscopic spinning behavior and the microscopic fiber morphology during the electrospinning process. As illustrated in **Fig. 2c**, the contents of the additive ($Fe(acac)_3$) and spinning aid (PVP) were independently varied within the ranges of 0 ~ 50 wt% and 0 ~ 100 wt%, respectively, relative to the weight of the precursor MK, thereby enabling gradient regulation of the solution viscosity and electrical conductivity. During electrospinning, the spinning behavior was comprehensively evaluated based on Taylor cone stability at the needle tip and the fiber microstructures observed by SEM. The spinning states were classified into five categories: unspinnable, discontinuous, uniform continuous, non-uniform continuous, and electrospray. Based on combined analysis of spinning stability and fiber morphology, the optimal electrospinning composition for SiOC fibers was identified, corresponding to a PVP content of approximately 20 ~ 50 wt% relative to the precursor and an additive content of 10 ~ 30 wt%.

Fig. S1 (Supporting Information**)** presents a comparison of the SEM images of pure SiOC fiber (without any addition of the $Fe(acac)_3$) and SF-1000, indicating the moderately balanced viscosity and conductivity favor the formation of nanostructures. The resultant SF-1000 nanofibers possess an average diameter of 670 nm, forming a 3D linear micro-network structure. However, the high carbon content in the SF-1000 nanofibers can enhance EMW attenuation upon incidence, thereby negatively impacting their wave-transmitting performance.[37] Therefore, oxidation treatment was applied to reduce the excess carbon content. As illustrated in **Fig. 2b**, a comparison of elemental compositions between SF-1000 and SFO-1000/1100/1200 indicates that the carbon content in SF-

Just Accepted

1000 was substantially reduced after oxidation, contributing to optimized wave-transmitting capability. To further verify the state of free carbon in different samples, Raman spectroscopic analysis was conducted and the results are presented in **Fig. S2**. For the SF-1000 sample, distinct characteristic peaks are observable at 1339 cm^{-1} and 1580 cm^{-1}, corresponding to the D-band and G-band of carbonaceous phases, respectively. This confirms the presence of free carbon in the unoxidized sample. However, no discernible carbon-related peaks are detected for the oxidized SFO-1000/1100/1200 samples, indicating that the oxidative treatment effectively consumes free carbon within the SiOC nanofibers. This depletion of free carbon plays a significant role in modulating the EMW-transmitting characteristics of the samples.

As shown in **Fig. 2e-g**, the 3D network structure of SiOC nanofibers remains intact after oxidation treatment. The average diameters of SFO-1000/1100/1200 are approximately 600, 460, and 430 nm, respectively. This size variation stems from the continuous carbon phase removal with increasing oxidation temperature. It is noteworthy that at excessively high oxidation temperatures (SFO-1200), the 3D architecture is partially disrupted due to fiber breakage, leading to a decline in mechanical performance. Furthermore, the fractured fibers generate numerous interfaces and cause additional EMW losses, which adversely affect EMW transmission properties. Corresponding to the variation patterns of solution viscosity and electrical conductivity in **Fig. 2a**, the diameter of $SF_{0.135}O$-1100/$SF_{0.27}O$-1100/$SF_{0.54}O$-1100 nanofibers gradually decreases from 520 to 400 nm (as shown in **Fig. S3-S4,** Supporting Information and **Fig. 2f**) as the $Fe(acac)_3$ addition amount increases (0.135, 0.27 and 0.54 g). This trend verifies the feasibility of achieving fiber nanosizing through the optimization of viscosity and conductivity.[38] However, at high iron content ($SF_{0.54}O$-1100), the significantly reduced viscosity and elevated conductivity increase the solution fluidity, leading to instability in the electrospinning jet and excessive stretching under the electric field. This, in turn results in fiber breakage. Additionally , the excessive Fe content introduces stronger magnetic loss, which compromises the wave-transmitting performance of the fiber membranes.[39]

High-resolution transmission electron microscopy (HRTEM) images of SF-1000 and SFO-1100 (**Fig. 2h**, **Fig. S5,** Supporting Information) reveal that no crystalized graphite lattice fringes are observed after oxidation, consistent with the EDS results in **Fig. 2b**. Most regions of the nanofibers exhibit an amorphous structure, corresponding to the amorphous SiOC matrix. XRD patterns (**Fig. 2i**) of SF-1000 and SFO-1000/1100 exhibit no distinct diffraction peaks except for a

Just Accepted

broad hump between 15° and 35°, characteristic of amorphous SiOC, [36] indicating that these samples are primarily in a low-crystallinity amorphous state. As the oxidation temperature increasing to 1200 ℃, the SFO-1200 sample exhibit pronounced peaks originates from the crystal planes of SiO_2 (JCPDS NO. 39-1425) (**Fig. S6,** Supporting Information). In addition, a small number of Fe_2O_3 nanocrystals, with a lattice spacing of 2.70 Å corresponding to the (104) plane of Fe_2O_3 (JCPDS NO. 33-0664).[40]

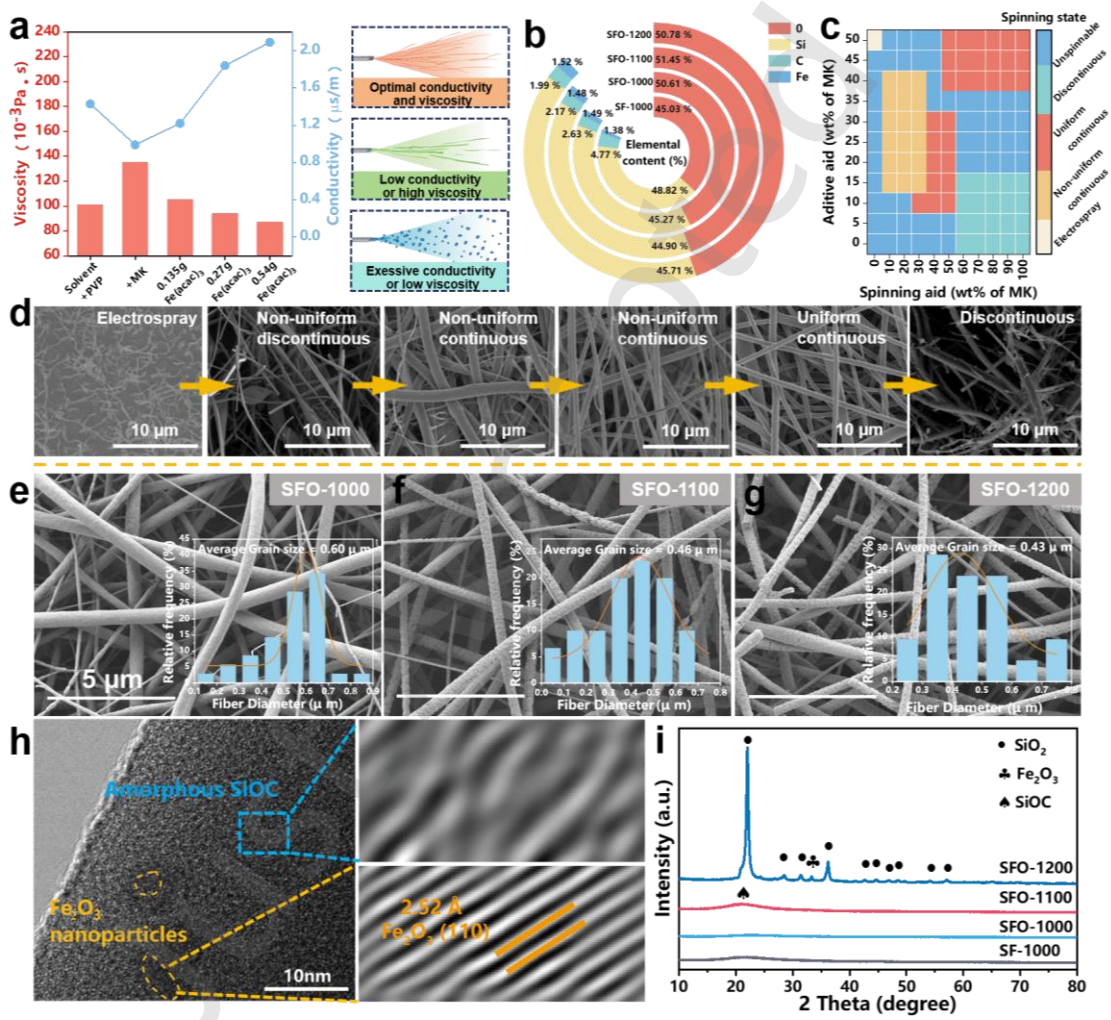


Fig. 2. (a) Effects of $Fe(acac)_3$ addition amount on the viscosity and conductivity of the electrospinning solution. **(b)** Elemental distributions of SF-1000 and SFO samples. **(c, d)** Illustration of the different spinning states and resultant sample morphologies obtained from electrospinning solution with varying ratios of spinning aid and additive. **(e)** SEM images of SFO-1000, **(f)** SFO-1100, and **(g)** SFO-1200. **(h)** HRTEM image and IFFT images of a single SFO-1100 nanofiber. **(i)** XRD patterns of SF-1000 and SFO samples.

3.2 Compressive resilience performance

The compressive resilience performance of the layered SF-1000 and SFO-1100 nanofiber

membranes is shown in **Fig. 3a-f**. With strain increasing from 20% to 60% (**Fig. 3a-b**), the reproducibility of peak stress values across consecutive loading cycles confirms the robust compressive recovery capabilities of both SF-1000 and SFO-1100. The oxidized membranes (SFO-1100) exhibit a higher density than SF-1000, which increases its resistance during compression. Consequently, SFO-1100 membranes demonstrate a significantly higher peak stress. At 60% compressive strain, the maximum stresses were recorded as 15 and 35 kPa for SF-1000 and SFO-1100, respectively, indicating that their structures can withstand compressive forces thousands of times their own weight while maintaining recovery ability. Furthermore, after three compression cycles at different strain levels, the curves exhibit good overlap, suggesting that the plastic deformation in SF-1000 and SFO-1100 is negligible (**Fig. S7 and S8**, Supporting Information). Meanwhile, the energy loss coefficient values at 60% strain are summarized (**Fig. S9**, Supporting Information) after three cycles, in which the coefficient drops obviously at 60% strain. This arises from the irreversible deformation or fracture of some nanofibers in high-strain regions, resulting in permanent structural damage. In this case, the strain of 50% is selected for the 500-cycle compression testing. As presented in **Fig. 3c-d**, the curves nearly overlap with the initial cycle, indicating excellent compressive resilience of both SF-1000 and SFO-1100. The inset of **Fig. 3c** shows the variation in maximum stress and energy loss coefficient during the compression cycles of SF-1000. As the number of cycles increased, the maximum stresses after 500 cycles remained at 95.7% of the original value, demonstrating good stability. On the other hand, the energy loss coefficient stabilized between 32% and 34%. Similarly, after 500 compression cycles, the maximum stresses of SFO-1100 remained at 93.1% of the original value, and the energy loss coefficients stabilized between 35% and 38% (inset of **Fig. 3d**). Meanwhile, stress-strain curves under 500-cycle compression at fixed stress values were also conducted and illustrated in **Fig. 3e-f**. After 500 cycles, the maximum strain value of SF-1000 extended from 53.02% to 54.75%. For SFO-1100, the value is from 50.13% to 52.05%. The minimal strain fluctuations observed during constant-stress cyclic compression demonstrate the robustness of the 3D network structure, which remained stable even after hundreds of compression cycles. However, as the oxidation temperature increases to 1200 ℃, the compressive resilience performance of SFO-1200 degrades substantially. As shown in **Fig. S10** (Supporting Information), the maximum stress declined more than 50% after 100 cycles. This failure is attributable to slight fiber breakage (**Fig. 2e**), which limits its practical applicability.

Just Accepted

The inherent flexibility of the amorphous nanofibers, combined with the micro-defects dispersed in the nanoscale fiber structure that create "buffer zones" to alleviate external stress, contributes to the excellent elastic compression performance of both samples.[41-43] The 3D network structure formed by the electrospinning technique enriches the nanofiber membranes with large porosity to provide enough space for deformation. During cyclic compression, energy loss arises mainly from two factors. First, elastic deformation of the nanofibers consumes energy. As the number of compressions increases, this energy consumption does not decrease, yielding a high energy loss coefficient even after 500 cycles. Second, relative sliding between nanofibers and the layers contributes to energy dissipation. Owing to residual strain, this energy remains at a consistent level.[44]

To further investigate the intrinsic mechanisms underlying the flexibility and compressive recovery of nanofiber membranes, in-situ scanning techniques were employed to observe morphological changes during bending. During bending deformation, the structural evolution of SFO-1100 was examined to understand the mechanism underlying its flexibility. SEM images in **Fig. 3g** reveal that the nanofiber membranes can endure extreme deformations corresponding to extremely small bending radius. The twisting and sliding of randomly oriented nanofibers within the membrane framework facilitate macroscopic deformation, effectively dispersing external forces across individual fibers and preventing stress concentration.[45] Despite the inherent rigidity of ceramic fibers, their high aspect ratio allows individual fibers to undergo slight angular deformations. As strain increases, the nanofiber membranes exhibit a characteristic curvature that gradually decreases without any signs of damage or fracture. Upon load releasing, the nanofibers recover their original shape, indicating excellent elasticity and flexibility. Therefore, the flexibility and compressive recovery of the SFO-1100 fiber membranes can be attributed to the motion and buckling of the modified SiOC nanofibers (**Fig. 3h**), originating from the three-dimensional network structure and the nanoscale features.[46]

Just Accepted

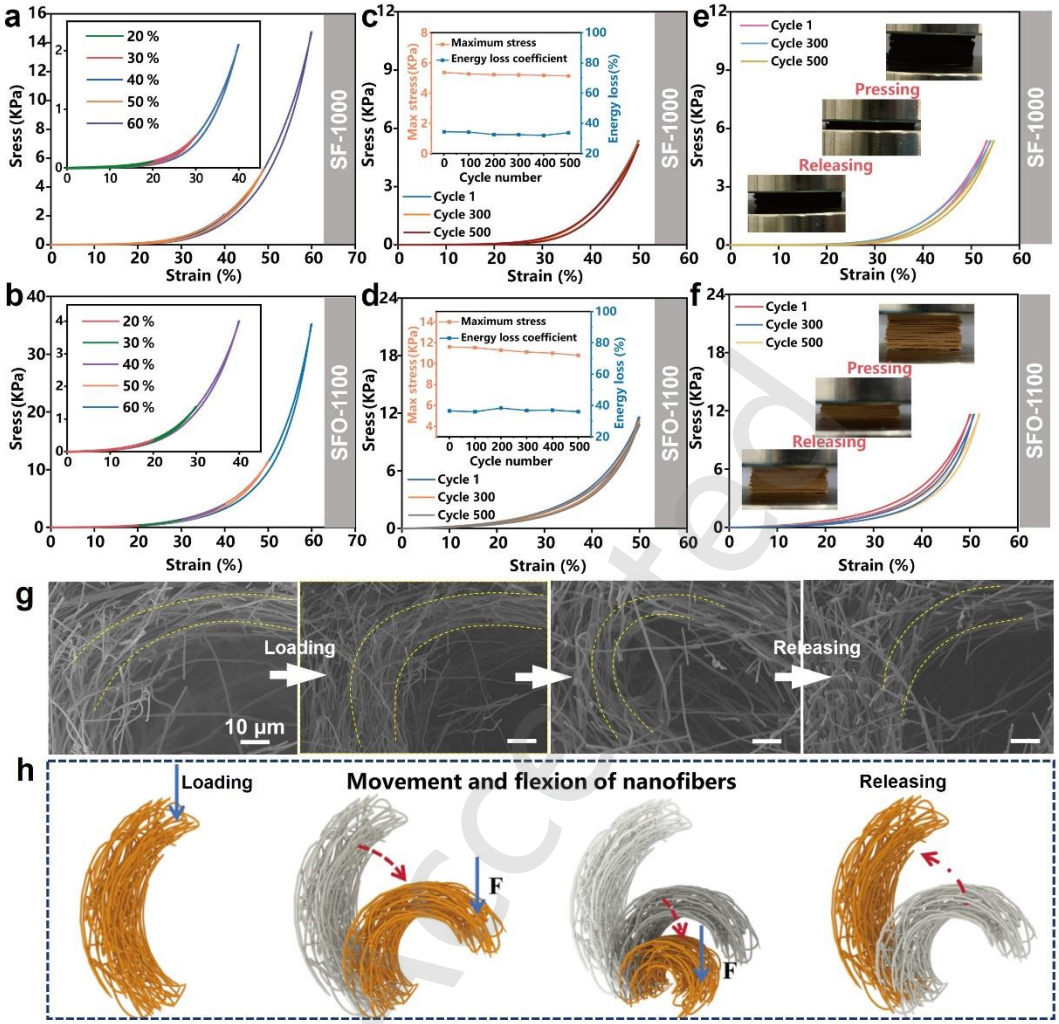


Fig. 3. **(a-d)** Stress-strain curves at strain ranges of 20% to 60%. **(c-d)** Stress-strain curves under cyclic compression at 50% strain (insets show the corresponding maximum stress and energy loss coefficient curves). **(e-f)** Stress-strain curves under cyclic compression at fixed stresses of 5.38 kPa (SF-1000) and 11.6 kPa (SFO-1100), respectively (insets show the compressive resilience process). **(g)** Microstructural changes of SFO-1100 during bending cycles. **(h)** Schematic model illustrating compression and release behavior of SiOC nanofibers, elucidating the elastic deformation mechanism.

3.3 Thermal insulation and pollutant adsorption performance

Thermal insulation tests were also conducted on SFO-1100 nanofiber membranes. As shown in **Fig. 4a**, an SFO-1100 sample with the thickness of 10 mm was tested on a hot plate at 250 °C. An infrared thermal camera recorded the temperatures to verify the actual thermal insulation performance. The surface temperature of the sample roses rapidly to 49.3 °C within 20s, stabilizing at approximately 60 °C after 20 min. **Fig. 4b** further illustrates thermal infrared images and real-time digital photographs of the 10 mm-thick SFO-1100 fiber membrane during butane torch exposure. Notably, the temperature on the front side of the membrane exceeded 450 °C when

directly exposed to the butane flame (top), whereas the back side remained significantly cooler at approximately 65 °C (bottom). Compared with SF-1000 sample, the average thermal conductivity (κ) of oxidized SFO-1100 sample decreased from 0.0398 $Wm^{-1}K^{-1}$ to 0.0362 $Wm^{-1}K^{-1}$, while the average density increased markedly from 50.05 $mg \cdot cm^{-3}$ to 69.23 $mg \cdot cm^{-3}$(**Fig. 4c**), which results from the increased oxygen content (**Fig. 2b**). In addition, the continuously heated beaker protected by a 10 mm-thick SFO-1100 insulation layer exhibited a significantly lower external temperature compared with the uncovered control (**Fig. 4d**). **Fig. 4e** further confirms this finding via infrared imaging, with the SFO-1100-covered region exhibiting a noticeably lower temperature. The hierarchical pore structure of the stacked nanofiber membrane presents a pronounced synergistic suppression effect on thermal conduction. *Firstly, the individual SiOC fibers possess rough surface with nanoscale open pores (**Fig. 2f**). According to the Nitrogen adsorption-desorption isotherm and pore size distribution curves in **Fig. S11**, the nanoscale pores are mainly distributed in the range of 10 ~ 100 nm (peaked at 65 nm), which are comparable to the mean free path of air molecules (~ 68 nm).* These pores trigger the Knudsen effect and thus markedly reduce gas convection and gaseous heat conduction. In addition, micron-scale pores between fibers within each membrane layer (1 ~ 5 μm) and the interlayer spaces formed naturally between stacked layers (>10 μm) create a hierarchical pore network (as shown in **Fig. S12**). This network lengthens the heat-flow path and introduces extra contact thermal resistance, as well as radiation-scattering interfaces at the layer boundaries. [47-49] Consequently, solid-phase conduction, gas-phase conduction, and interfacial thermal coupling are simultaneously attenuated within this hierarchical structure, enabling the stacked nanofiber membrane to achieve superior thermal-insulation performance compared with single-scale porous architectures while maintaining an exceptionally low overall density.

The compressive strength of the SFO-1100 nanofiber membranes was also evaluated under high-temperature calcination conditions. **Fig. 4f** shows the in-situ performance of SFO-1100 under continuous heating with an alcohol lamp while applying compressing and bending forces. No damage or cracks were observed, indicating that the internal structure of the SFO-1100 nanofiber membrane remains intact even after prolonged high-temperature exposure. After 5 min of direct flame exposure, the maximum stress during the first compression cycle at a 50% strain remains at 11.3 kPa, representing a decrease of only 2.6% compared to the untreated SFO-1100 (**Fig. S13-S14**, Supporting Information). After 300 compression cycles, the maximum stress of the flame-treated

Just Accepted

sample reached 95.4% compared with the untreated sample, and the energy loss coefficient slightly increased to 38.36% (**Fig. 4g**, **Fig. S14**, Supporting Information).

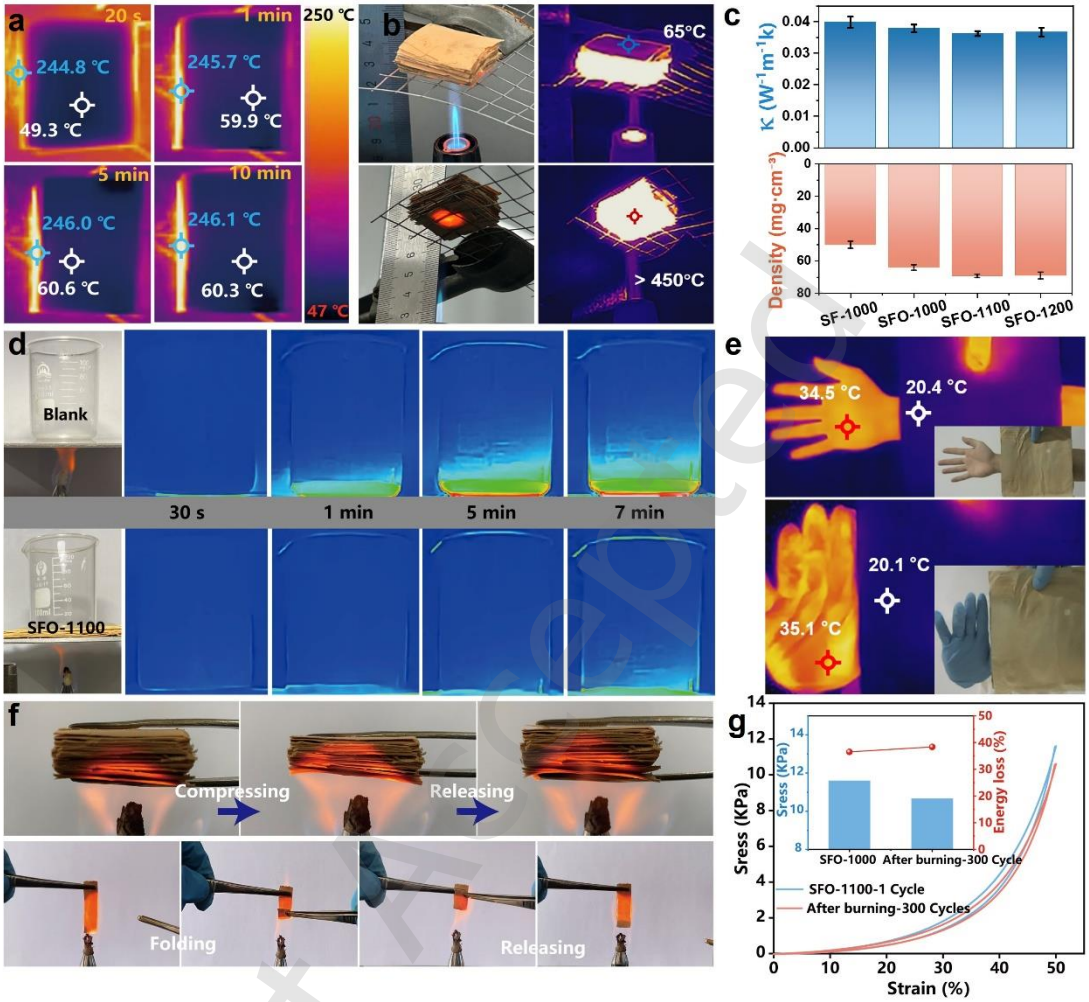


Fig. 4. **(a)** Infrared images of SFO-1100 on a 250 °C heating platform. **(b)** Digital photograph and infrared images of the SFO-1100 under butane torch heating, showing the front view (top) and back view (bottom). **(c)** Comparison of average thermal conductivity and density between SF-1000 and SFO nanofiber membranes. **(d)** Infrared images during alcohol lamp burning, showing the blank control (top) and the area covered by SFO-1100 (bottom). **(e)** Infrared image of an SFO-1100 sample attached to the human arm. **(f)** Digital photographs of compression and bending performance tests on SFO-1100 during flame heating. **g)** Compressive cycling curves of SFO-1100 after flame treatment, along with the corresponding peak compressive stress and energy loss coefficient over 300 compression cycles.

EM transparent ceramic components are frequently deployed in contaminated environments where exposure to organic vapors, oils, dust, and hydrocarbon deposits is unavoidable. Accumulation of these contaminants on the material surface progressively alters the local dielectric environment, increasing surface conductivity and dielectric constant, which in turn affects impedance matching and EM transmission efficiency. Thanks to the hierarchical porous architecture,

Just Accepted

the SFO-1100 nanofiber membrane provides an active barrier that captures pollutants within its pore channels before they reach the underlying functional surface. The adsorbed organic reagents can also be recovered through direct combustion of the membranes (**Fig. 5a**), while heat treatment in a furnace at 500 ℃ for 10 min achieves a similar regeneration effect (**Fig. 5b**). **Fig. 5c** further compares the mass variation of nanofiber membranes during adsorption and thermal treatment cycles with various pollutants. The results indicate that after ten consecutive adsorption–treatment cycles, the SFO-1100 membranes retain their adsorption capacity with negligible loss. The detailed mass and the corresponding absorption capacity of the adsorption–combustion process is presented in **Fig. 5d-e**. The as-prepared nanofiber membranes exhibit excellent adsorption performance and stability, with adsorption capacities for both ethanol and dye reaching approximately 8000 mg/g. Notably, no significant attenuation is observed after ten adsorption–desorption cycles, further confirming the robustness of the material. Consistent with these findings, no significant changes are observed in membrane mass or in ethanol adsorption capacity after repeated cycling. The high surface area and porosity of SFO-1100 nanofibers facilitate the efficient adsorption of organic dyes and pollutants, while their thermal stability ensures low degradation and excellent recyclability during high-temperature cycling (**Fig. 5f**) [50] Thus, the integration of recyclable pollutant capture with stable EM transmission creates a self-maintaining, long-service-life platform that is particularly advantageous for extreme-environment applications where routine replacement or cleaning of EMW-transparent components is impractical.

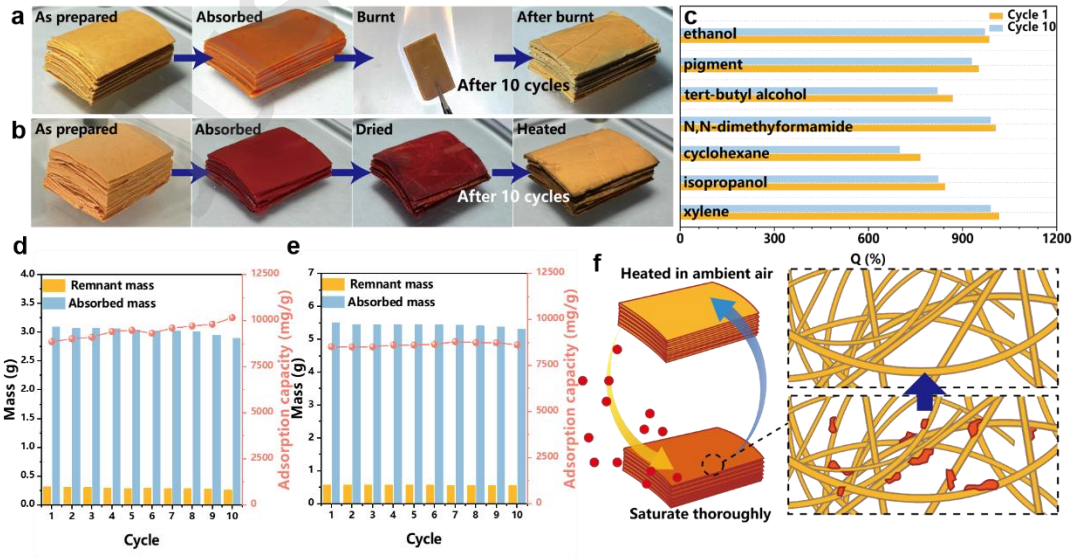


Fig. 5. Cyclic adsorption–elimination process of SFO-1100 for **(a)** organic contaminants and **(b)** pigment.

(c) Comparison of the absorption capacity of SFO-1100 for various organic liquids between the first and tenth cycles. Recyclability of SFO-1100 demonstrated by **(d)** ethanol absorption via direct combustion and **(e)** dye absorption via evaporation. **(f)** Schematic illustration of pollutant adsorption–elimination mechanisms by SFO-1100.

3.4 EMW transmission performance

Fig. 6a-b compare the real parts of the complex permittivity (ε′) and dielectric loss values (tanδ = ε″/ε′) for SF-1000 and SFO-1000/1100 nanofiber membranes. Insufficient oxidation of SF-1000 and SFO-1000 nanofibers leads to carbon residue resulting in elevated ε′ and tanδ values. Notably, the SFO-1100 sample shows stable ε′ and tanδ values within the relatively low ranges of 1.008–1.01 and 0.0004–0.0023, respectively. The ultra-low dielectric constant and loss tangent of SFO-1100 nanofiber membranes are essential for high-quality wave-transmitting materials, minimizing EM reflection and loss. Equations (S2-S4) (**Supporting Methods**, Supporting Information) characterize EMW transmission performance by calculating the wave transmission efficiency (T) of SF-1000 and SFO-1000/1100 samples from their S-parameters. As shown in **Fig. 6c** and **Fig. S15** (Supporting Information), SFO-1100 exhibits the highest wave transmission performance. The T value of SFO-1100 exceed 99% within the whole frequency range (8.2-12.4 GHz), indicating excellent wave transparency. As previously mentioned, the sample with excessive iron content ($SFO_{0.54}$-1100) exhibits noticeable magnetic loss, which consequently weakens the wave-transmitting performance (**Fig. S16**, Supporting Information). Consequently, stringent control over Fe_2O_3 nanoparticle loading is imperative to achieve synergistic compatibility between fiber nanoscaling and EMW-transmitting performance. In the optimized SFO-1100 formulation, the Fe content is maintained at an extremely low level (Fe weight ratio < 1.5 wt% by EDS), with Fe species sparsely dispersed throughout the amorphous SiOC matrix. Under such dilute conditions, the percolation threshold for conductive/magnetic loss networks remains unattained. More significantly, the decisive factor governing EM transmission is the effective elimination of free carbon, which would otherwise establish high-dielectric-loss pathways.

To further elucidate the ability of EMW to enter the materials, the normalized input impedance ratio $|Z_{in}/Z_0|$[51-53] was introduced. Compared with SF-1000, the SFO series exhibits significantly improved impedance matching characteristics, as evidenced by the expanded matching bandwidth, enlarged matching region, and enhanced thin-layer matching capability, thereby enabling more incident EMW to penetrate into the materials. This observation is consistent with the superior wave-

Just Accepted

transmission performance of the SFO series discussed above. (**Fig. S17**, Supporting Information).

To verify the stable EMW transmission performance under harsh conditions, transmission tests were also conducted on SFO-1100 samples that had undergone both flame treatment (5 mins) and cyclic compression treatment (500 times). As shown in **Fig. 6d**, the ε′ (below 1.02) and tanδ (below 0.0045) values of the treated SFO-1100 samples remained at low levels. Consequently, the T values of the treated nanofiber membranes were above 98% in the 8.2-12.4 GHz frequency range, comparable to those of freshly prepared samples. In addition, the flexibility of the SFO-1100 nanofiber membrane was further evaluated through a 180° cyclic bending test conducted over 500 cycles. As shown in **Fig. S18** (Supporting Information), the T recorded after 1, 100, 300, and 500 cycles exhibit only a slight reduction following 300 cycles. Significantly, the average T value remains above 0.985 even after 500 cycles, underscoring the excellent flexibility and stable EMW transmission capability of the nanofiber membrane under repeated deformation. These results highlight potential for applications in high-temperature and harsh environments. **Fig. 6e–f** presents the in-situ waveguide measurement results during heating from room temperature (RT) to 873 K. As the temperature increases, the tanδ in the range of 473 ~ 673 K shows minimal variation (< 0.005) compared to RT, maintaining an ultra-low-loss characteristic comparable to that of air. At 873 K, the tanδ increases slightly but remains at the level of ~ 0.01, still indicating negligible dielectric loss. The gradual increase in tanδ with temperature can be attributed to reduced relaxation time. According to the Debye relaxation model, elevated temperature accelerates dipolar polarization dynamics, leading to shorter relaxation times and consequently enhanced dielectric response[54]. **Fig. 6f** further illustrates the temperature-dependent evolution of the T values, confirming the excellent high-temperature wave-transmitting stability of SFO-1100. Below 673 K, T remains nearly unchanged compared to RT, consistently exceeding 0.99. Although a more pronounced decrease is observed at 873 K, the T value still exceeds 0.985, demonstrating the outstanding thermal stability and low-loss EM transparency of the material at elevated temperatures. The outstand EMW transmission performance of SFO-1100 nanofibers could be attributed to three aspects (**Fig. 6g**): Firstly, the amorphous SiOC phase with low crystallinity exhibits low intrinsic permittivity and weak dielectric attenuation. Secondly, high-temperature oxidation substantially reduces the high-loss free-carbon phase within the nanofibers. Thirdly, the unique porous and loose structure formed by the 3D distribution of nanofibers allows more air to be distributed in the internal spaces, thereby

Just Accepted

contributing to favorable impedance matching and a low dielectric constant.

The multifunctional integration exhibited by the present amorphous SiOC nanofiber membrane represents a deliberate departure from conventional ceramic design paradigms. Traditional dense wave-transparent ceramics, such as hot-pressed Si_3N_4 [3] and Al_2O_3, [5] achieve acceptable electromagnetic transmission yet suffer from densities exceeding 2.0 g/cm^3 and inherent brittleness that preclude conformal deployment. Conversely, existing PDCs materials, [37, 55] have predominantly been engineered for EM absorption or high-temperature structural stability, where the deliberate retention of free carbon and crystalline phases enhances dielectric/magnetic losses at the expense of transmission efficiency. By contrast, the strategy developed herein, combining modified electrospinning with controlled post-pyrolysis oxidation, enables the intentional elimination of lossy free-carbon phases while preserving the amorphous SiOC backbone within an ultralight fibrous architecture. This approach yields three synergistic advantages. Architecturally, the 3D porous nanofiber network simultaneously endows mechanical flexibility through inter-fiber sliding and elastic bending, thermal insulation via air entrapment and suppressed solid-phase conduction, and excellent EM transparency through a low effective dielectric constant and favorable impedance matching. Compositionally, oxidative removal of conductive carbonaceous phases drastically reduces dielectric loss to enable ultralow-loss wave transmission, while the enriched Si–O surface terminations concurrently enhance hydrophilicity for pollutant adsorption. Microstructurally, the amorphous nature of the SiOC matrix avoids grain-boundary fracture to ensure mechanical compliance and suppresses interfacial polarization losses typical of crystalline ceramics. Consequently, this harmonious convergence of structural porosity, compositional tuning, and microstructural disorder achieves the monolithic integration of EM transparency, thermal insulation, mechanical resilience, and recyclable pollutant adsorption, overcoming the historical trade-offs between density, flexibility, and low-loss performance that constrain both traditional ceramics and conventional PDC systems.

Fig. 6h presents the relatively low ε' and tanδ values of SFO-1100, which are lower than those of most previously reported wave-transmitting materials, such as Si_3N_4 nanobelt aerogels, Si_3N_4-based composites, SiO_2 composites, SiAlO based composites, silicone-based polymers and their derivatives (**Table S1**, Supporting Information). A radar chart provides a detailed comparison of the comprehensive performance of SFO-1100 nanofiber membranes with reported transparent materials

Just Accepted

regarding maximum operating temperature in air, lightweight characteristics, flexibility, compressive resilience, wave transparency, and thermal insulation performance (**Fig. 6i, Table S2**, Supporting Information). The outstanding overall performance is primarily attributed to the low-dielectric amorphous SiOC phase, the one-dimensional and nano-scale nature of the fibers, and the unique porous structure of the nanofiber membranes. Specifically, SFO-1100 nanofiber membranes demonstrate high operating temperatures, excellent compressive resilience, superior wave transparency, low density, and exceptional thermal insulation. Notably, the flexibility and recyclability of SFO-1100 nanofiber membranes provide a significant advantage over other wave-transparent materials in demanding application environments.

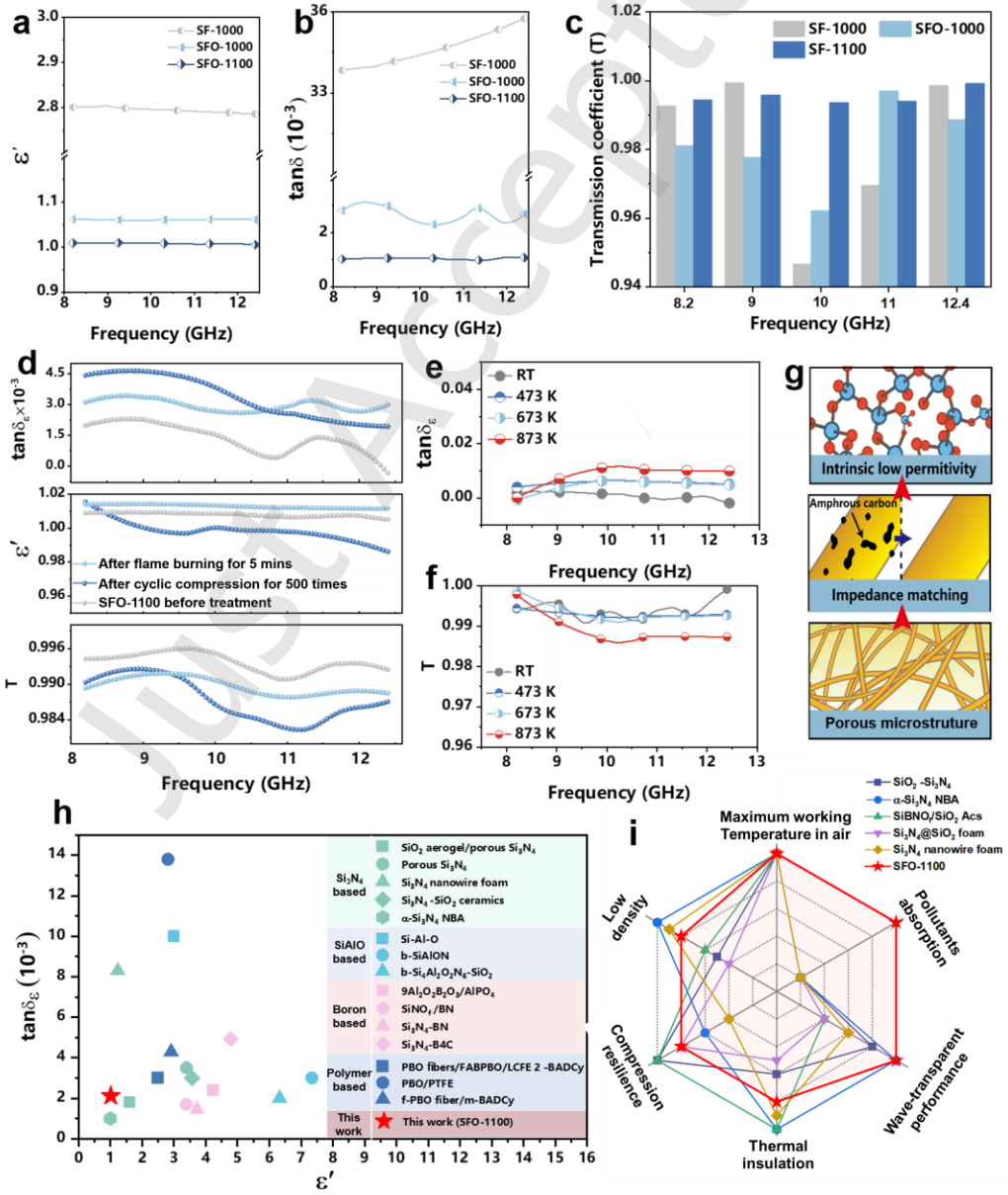


Fig. 6. Frequency-dependent **(a)** real part of permittivity (ε′), **(b)** dielectric loss (tanδ), and **(c)**

transmission coefficient (T) of SF-1000 and SFO samples. **(d)** ε′, tanδ and T of SFO-1100 after flame burning and cyclic compression treatment. In-situ variation of **(e)** tanδ and **(f)** T for SFO-1100 from room temperature to 873 K. **(g)** Schematic diagram illustrating the EMW transmission mechanism. **(h)** Comprehensive comparison of reported wave-transparent materials in terms of ε′ and tanδ. **(i)** Radar chart displaying overall performance comparison of the samples in this study with other reported wave-transparent materials.

4. Conclusion

In this study, flexible amorphous SiOC nanofiber membranes were fabricated via electrospinning coupled with high-temperature oxidation. The exceptional EMW transmission originates from the intrinsically low polarizability of the amorphous SiOC matrix, the oxidative elimination of free carbon, and the impedance-matching porous 3D nanofiber network that embeds abundant low-permittivity air. Concurrently, the resultant SiOC membrane exhibits an exceptional combination of multi-functional performance, including outstanding compressive elasticity (with a stress retention >95% after 500 compression cycles at 50% strain), ultralow thermal conductivity (<0.04 $W \cdot m^{-1} \cdot K^{-1}$), excellent fire resistance (maintaining structural integrity after fired for 5 mins), and good recyclability (negligible mass and performance loss after 10 pollutant adsorption–removal cycles). Furthermore, these membranes achieve an ultralow dielectric constant ($\varepsilon' \approx 1.0$) and loss tangent ($\tan\delta < 0.0023$), enabling excellent EMW transparent performance. Compared with conventional EM-transmitting ceramics, the amorphous SiOC nanofibers synthesized in this study overcome the trade-off between high-temperature mechanical stability and low dielectric loss, offering a promising pathway toward multifunctional integrated wave-transmitting materials for use in extreme environments.

Just Accepted

Acknowledgements

The authors thank the National Natural Science Foundation of China (Youth Project 52402362, General Program 12374394)，Youth Project of Natural Science Foundation of Jiangsu Province (BK20230341).

5. Reference

1. Wang X, Duan W, Li S, et al. Preparation of Si_3N_{4f}/Si_3N_4 wave-transparent composites by vat photopolymerization combined with chemical vapor infiltration. *Addit Manuf* 2024, **95:** 104540.

2. Tang L, Zhang J, Tang Y, et al. Polymer matrix wave-transparent composites: A review. *J Mater Sci Technol* 2021, **75:** 225-251.

3. Cheng Z, Ye F, Liu Y, et al. Mechanical and dielectric properties of porous and wave-transparent Si_3N_4-Si_3N_4 composite ceramics fabricated by 3D printing combined with chemical vapor infiltration. *J Adv Ceram* 2019, **8:** 399-407.

4. Xie Z, Tang Y, Luo Z, et al. Dual metal synergistic modulation of boron nitride for high-temperature wave-transparent metamaterials. *Mater Horiz* 2025, **12:** 1547-1557.

5. Li D, Jia D, Yang Z, et al. Principles, design, structure and properties of ceramics for microwave absorption or transmission at high-temperatures. *Int Mater Rev* 2022, **67:** 266-297.

6. Wang J, Li Y, Cao J, et al. Robust and thermally insulating SiBCN/SiOC ceramic aerogel with superior electromagnetic wave absorption performance and high-temperature stability up to 1600 °c. *J Adv Ceram* 2026, **15:** 9221256.

7. Jiang J, Yan L, Xue Y, et al. Lightweight and thermally insulating polymer-derived $SiBCN/SiCN_w$ ceramic aerogel with enhanced electromagnetic wave absorbing performance. *Chem Eng J* 2024, **482:** 148878.

8. Guo C, Ye F, Cheng L. In situ growth of single crystal Si_3N_4 nanowire foam with good wave-transparency and heat insulation performance. *Compos Part B-Eng* 2021, **224:** 109129.

9. Yin X, Kong L, Zhang L, et al. Electromagnetic properties of Si–C–N based ceramics and composites. *Int Mater Rev* 2014, **59:** 326-355.

10. Lu K, Erb D. Polymer derived silicon oxycarbide-based coatings. *Int Mater Rev* 2018, **63:** 139-161.

11. Chen Z, Liu S, Wu Y, et al. Recent progress in silicone foams and nanocomposites: From versatile fabrication strategies to multiple emerging applications. *Nano Mater. Sci.* 2025,

12. Zhou S, Zhao Y, Guo X, et al. Corrosion-resistant and heat-dissipative SiOC ultralight lattice for high-temperature emi shielding. *Addit Manuf* 2025, **111:** 104964.

13. Lin Y, Fan X, Tang L, et al. Polysilsesquioxane-PBO wave-transparent composite paper with excellent mechanical properties and ultraviolet aging resistance. *Adv Fiber Mater* 2023, **5:** 2114-2126.

14. Tang L, Tang Y, Zhang J, et al. High-strength super-hydrophobic double-layered PBO nanofiber-polytetrafluoroethylene nanocomposite paper for high-performance wave-transparent applications. *Sci Bull* 2022, **67:** 2196-2207.

15. Pan L, Liu R, Meng F, et al. Flexible and resilient Co/TiO_2/SiOC nanofibers via electrospinning: Towards thermal and electromagnetic wave protection. *J Adv Ceram* 2024, **13:** 1666-1676.

16. Feng Y, Guo X, Huang K, et al. Enhanced electromagnetic microwave absorption of SiOC ceramics targeting the integration of structure and function. *J Eur Ceram Soc* 2021, **41:** 6393-6405.

17. Stabler C, Ionescu E, Graczyk-Zajac M, et al. Silicon oxycarbide glasses and glass-ceramics: "All-rounder" materials for advanced structural and functional applications. *J Am Ceram Soc* 2018, **101:** 4817-4856.

18. Hernandha RFH, Umesh B, Patra J, et al. Core-shell Si@SiOC particles synthesized using supercritical carbon dioxide fluid for superior li-ion storage performance. *Adv Sci* 2024, **11:** 2401350.

19. Ackley BJ, Martin KL, Key TS, et al. Advances in the synthesis of preceramic polymers for the

Just Accepted

formation of silicon-based and ultrahigh-temperature non-oxide ceramics. *Chem Rev* 2023, **123:** 4188-4236.
20. Wang X, Zhu Z, Guo Z, et al. Thermally insulating and wave-transparent magnesium aluminum spinel nanofibers applied from − 196 to 1600 ℃. *Chem Eng J* 2024, **502:** 157617.
21. Meng X, Yu M, Wang C. The design of ternary nanofibers with core–shell structure for electromagnetic stealthy antenna. *Adv Fiber Mater* 2024, 1-12.
22. Song L, Wang L, Chen Y, et al. Engineered core–shell SiC@SiO_2 nanofibers for enhanced electromagnetic wave absorption performance. *Small* 2024, **20:** 2407563.
23. Guo X, Wang H, Xing P, et al. Organosilane waste-derived SiC_{nws}/SiOC composites with enhanced electromagnetic wave absorption performance. *Ceram Int* 2024, **50:** 8269-8276.
24. Ji D, Lin Y, Guo X, et al. Electrospinning of nanofibres. *Nat Rev Methods Primers* 2024, **4:** 1.
25. Liu JH, Wang P, Gao Z, et al. Review on electrospinning anode and separators for lithium ion batteries. *Renew Sust Energy Reviews* 2024, **189:** 113939.
26. Long K, Cui Y, Meng H, et al. ZnO nanofiber derived from Zinc loaded chitosan nanofiber as an efficient adsorbent for congo red from aqueous solution. *J Inorg Organomet P* 2025, **35:** 317-325.
27. Wen J, Li K, Xu K, et al. Preparation of flexible porous γ-Al_2O_3 nanofibers by electrospinning and its application in supercapacitor separator. *J Solid State Electrochemi* 2024, **28:** 4325-4338.
28. Lee J, Yoon J, Oh S-G. Electrospun nanofiber-based tri-layer separators with CuO/TiO_2 nanowires for high-performance and long-cycle stability of lithium-ion batteries. *J Ind Eng Chem* 2024, **135:** 165-174.
29. Zhou Q, Sun Y, Li Z, et al. Preparation of CS/PVA/POP nanofiber membranes and adsorption behavior for Hg (ii) ions. *Water* 2025, **17:** 885.
30. Liu H, Jin L, Zhu S, et al. Motion-activating pliable carbon nanofiber for smart mechanosensitive sensing and antibacterial protection. *Adv Funct Mater* 2025, **35:** 2415258.
31. Zhao Y, Zhang Y, Yang C, et al. Ultralight and flexible SiC nanoparticle-decorated carbon nanofiber mats for broad-band microwave absorption. *Carbon* 2021, **171:** 474-483.
32. Zhang Y, Liu S, Yan J, et al. Superior flexibility in oxide ceramic crystal nanofibers. *Adv Mater* 2021, **33:** 2105011.
33. Wu F, Qiang S, Zhang X, et al. The rising of flexible and elastic ceramic fiber materials: Fundamental concept, design principle, and toughening mechanism. *Adv funct mater* 2022, **32:** 2207130.
34. Gradinaru LM, Bercea M, Vlad S, et al. Preparation and characterization of electrospun magnetic poly(ether urethane) nanocomposite mats: Relationships between the viscosity of the polymer solutions and the electrospinning ability. *Polymer* 2022, **256:** 125186.
35. Wang C, Wang W, Qi H, et al. Electrospinning and electrospun nanofibers: From academic research to industrial production. *Prog Mater Sci* 2025, 101494.
36. Hou Y, Cheng L, Zhang Y, et al. Enhanced flexibility and microwave absorption properties of HfC/SiC nanofiber mats. *ACS Appl Mater Interfaces* 2018, **10:** 29876-29883.
37. Yu Z, Lv X, Mao K, et al. Role of in-situ formed free carbon on electromagnetic absorption properties of polymer-derived SiC ceramics. *J Adv Ceram* 2020, **9:** 617-628.
38. Peterson GW, Epps TH. Impact of zinc salt counterion on poly(ethylene oxide) solution viscosity, conductivity, and ability to generate electrospun MOF/nanofiber composites. *Polymer* 2022, **252:** 124816.
39. Ma Y, Yang F, Kou S, et al. Enhanced microwave absorption properties of Fe-doped SiOC ceramics by the magnetic-dielectric loss properties. *Ceram Int* 2021, **47:** 24393-24402.
Just Accepted

40. Song G, Wei M, Zhou J, et al. Modulation of the phase transformation of Fe_2O_3 for enhanced water oxidation under a magnetic field. *ACS Catalysis* 2024, **14:** 846-856.
41. Zhang X, Yu J, Zhao C, et al. Engineering covalent heterointerface enables superelastic amorphous SiC meta-aerogels. *ACS Nano* 2023, **17:** 21813-21821.
42. Zhang M, Xu W, Ma C-L, et al. Highly active and selective electroreduction of N_2 by the catalysis of Ga single atoms stabilized on amorphous TiO_2 nanofibers. *ACS Nano* 2022, **16:** 4186-4196.
43. Qiang S, Wu F, Liu H, et al. Integration of high strength, flexibility, and room-temperature plasticity in ceramic nanofibers. *Nat Commun* 2025, **16:** 3265.
44. Wang X, Zhang Y, Zhao Y, et al. A general strategy to fabricate flexible oxide ceramic nanofibers with gradient bending-resilience properties. *Adv Funct Mater* 2021, **31:** 2103989.
45. Xu M, Futaba DN, Yamada T, et al. Carbon nanotubes with temperature-invariant viscoelasticity from –196° to 1000 ℃. *Science* 2010, **330:** 1364-1368.
46. Zhao K, Zhang T, Chang H, et al. Super-elasticity of three-dimensionally cross-linked graphene materials all the way to deep cryogenic temperatures. *Sci Adv* 2019, **5:** eaav2589.
47. Chen X, Zhang Z, Hu C, et al. Thermal insulation nanofiber aerogels: A journey from structure construction to multifunctionalization. *Small* 2025, **21:** 2502291.
48. Tian Y, Chen Y, Wang S, et al. Ultrathin aerogel-structured micro/nanofiber metafabric via dual air-gelation synthesis for self-sustainable heating. *Nat Commun* 2024, **15:** 6416.
49. Li J, Hu X, Pan Y, et al. Mechanically robust and thermal insulating silica/aramid nanofiber composite aerogel fibers with dual networks for fire-resistant and flexible triboelectric nanogenerators. *Adv Funct Mater* 2024, **34:** 2410940.
50. Jia C, Xu Z, Luo D, et al. Flexible ceramic fibers: Recent development in preparation and application. *Adv Fiber Mater* 2022, **4:** 573-603.
51. Jia Z, Guo Z, Ma H, et al. Polymetallic cation doping induced vacancy engineering for synergistically enhanced electromagnetic wave absorption. *Carbon* 2026, **251:** 121357.
52. Zhou J, Huang X, Lan D, et al. Multi-interface polarization engineering constructs one-dimensional carbon nanocages heterostructures for efficient electromagnetic wave absorption. *Carbon* 2026, **248:** 121143.
53. Wei H, Lai Y, Chen S, et al. Phase-transition-mediated dual-path optimization in SiC_{nws}@TiO_2 aerogels for synergistic microwave absorption and thermal insulation. *J Mater Sci Technol* 2026, **268:** 114-123.
54. Cao M, Song W, Hou Z, et al. The effects of temperature and frequency on the dielectric properties, electromagnetic interference shielding and microwave-absorption of short carbon fiber/silica composites. *Carbon* 2010, **48:** 788-796.
55. Zhou C, Wei Z, Yun F, et al. Polymer-derived C_f/C/SiC ceramic aerogel composites with superior microwave absorption properties. *Ceram Int* 2026, **52:** 8162-8171.

Just Accepted